LBNL FORGE Project 3-2535 Task 3 Milestone Report 3.1

Development of a Reservoir Seismic Velocity Model

Roland Gritto, Array Information Technology, Berkeley, CA

Don Vasco, Earth and Environmental Sciences, Lawrence Berkeley National Laboratory, Berkeley, CA

Coral Chen, University of California, Berkeley, CA

1. Introduction

In FORGE project 3-2535, Array Information Technology (AIT) and Lawrence Berkeley National Lab (LBNL) are planning to develop a representative 3D seismic velocity model in support of future research activities. Seismic velocities for the 3D model will be taken from seismic reflection profiling and available well logs, obtained during prior FORGE phases. As such, the model will combine a combination of different measurements and datasets and will be updated as more data become available. Modeling seismic wave propagation associated with the seismicity recorded during Phase III of the April 2022 FORGE stimulation in well 16A(78)-32 will be conducted to investigate the dependence of the resolution of the seismic waves in the stimulated volume on the geometry of seismic and DAS sensor arrays. The goal is to optimize usage of the available sensor data to provide the best resolution in the targeted fracture volume. This will reveal whether future seismic imaging campaigns will be able to reliably image the stimulated reservoir volume. Furthermore, the outcome could be used to optimize the number and the experimental geometry for the placement of seismic sensors during the upcoming stimulation in well 16B(78)-32. In the following, we will describe the progress in the development of the velocity model and report first results of our seismic resolution analysis.

2. Development of a Reservoir Seismic Velocity Model (Task 3.1)

During the exploration phase of the FORGE site in Milford, UT, a seismic reflection survey was conducted to image the subsurface geology, including the sedimentary overburden and the granitic basement (Miller, 2019). The reflection survey consisted of 986 vibroseis source locations and 1,740 geophone receivers. The geometry of the survey is shown in Figure 1, where the source and geophone positions are given by the open black circles and black dots, respectively. The development of the initial velocity model was based on RMS velocities of the reflection survey, which were scaled to match the observed velocities obtained by seismic logging in the shallow sedimentary section and in the underlaying basement rock. The velocities in the sedimentary layers were derived from a vertical seismic profiling (VSP) survey recorded by a distributed acoustic sensing (DAS) string, while the velocities in the basement were obtained by sonic logging in well 78B-32. The velocity profile of the initial model, scaled to the shallow and deep velocity logs, is presented in Figure 2. After scaling, the initial model fits the logging velocities quite well.
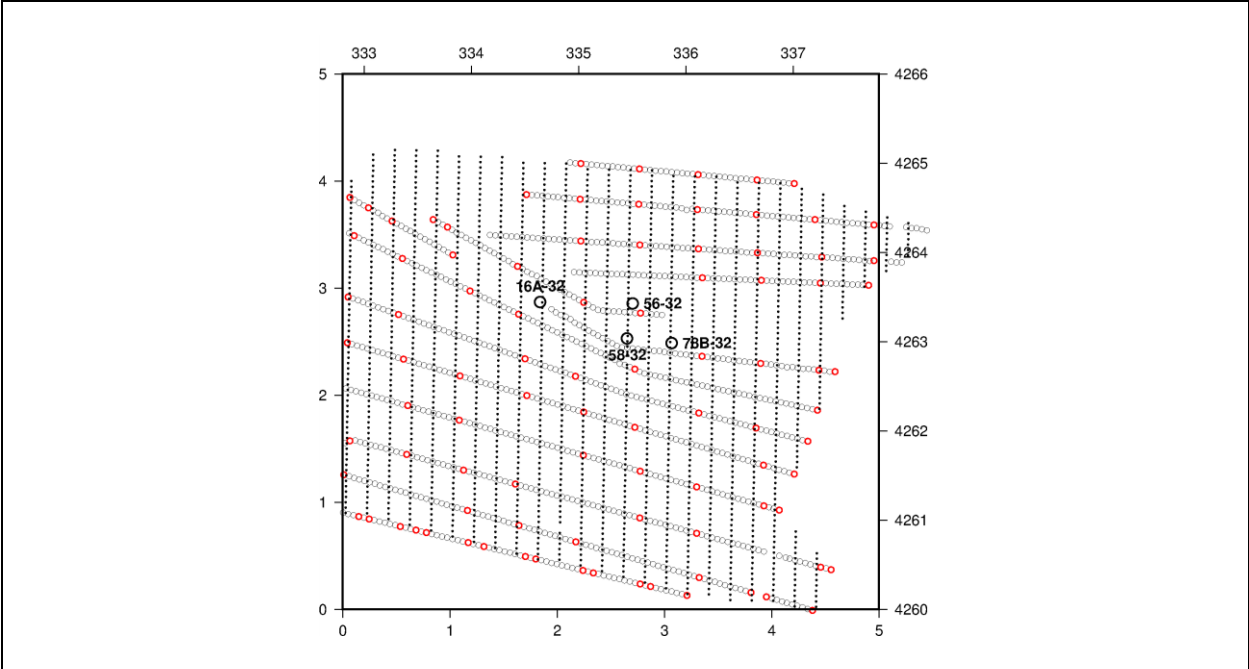
Figure 1. Map of the FORGE area with the geometry of the seismic reflection survey. The vibroseis source locations and geophone positions are given, respectively, by the open black circles and black dots. The open red circles represent a subset of source positions, for which travel times of the direct P-wave were determined using a deep-neural network algorithm. The FORGE wells are shown for reference.
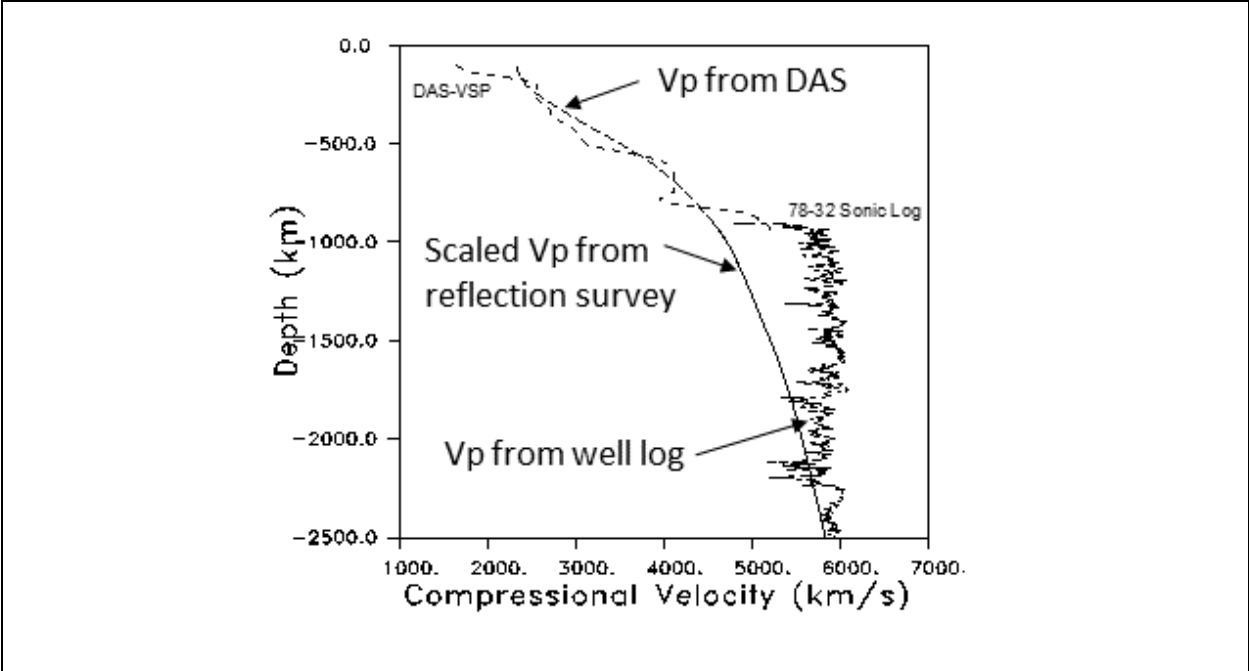

Figure 2. Profiles of the P-wave velocities derived from the reflection survey, the VSP experiment recorded by DAS, and the sonic logging in well 78B-32. The velocity profile from the reflection survey was scaled by a factor of 1.4 to match velocities observed in the boreholes.

2

The scaled velocity model obtained from the seismic reflection survey is shown in Figure 3. The sediments, represented by P-wave velocities from 3.0 km/s to 4.5 km/s, are slightly dipping to the West. The basement interface is represented by a velocity increase to 5 km/s at a depth of approximately 1 km. In this model, basement velocities are increasing from 5 km/s to 6 km/s at depth, with the FORGE reservoir located within rocks in the upper 5km/s range.
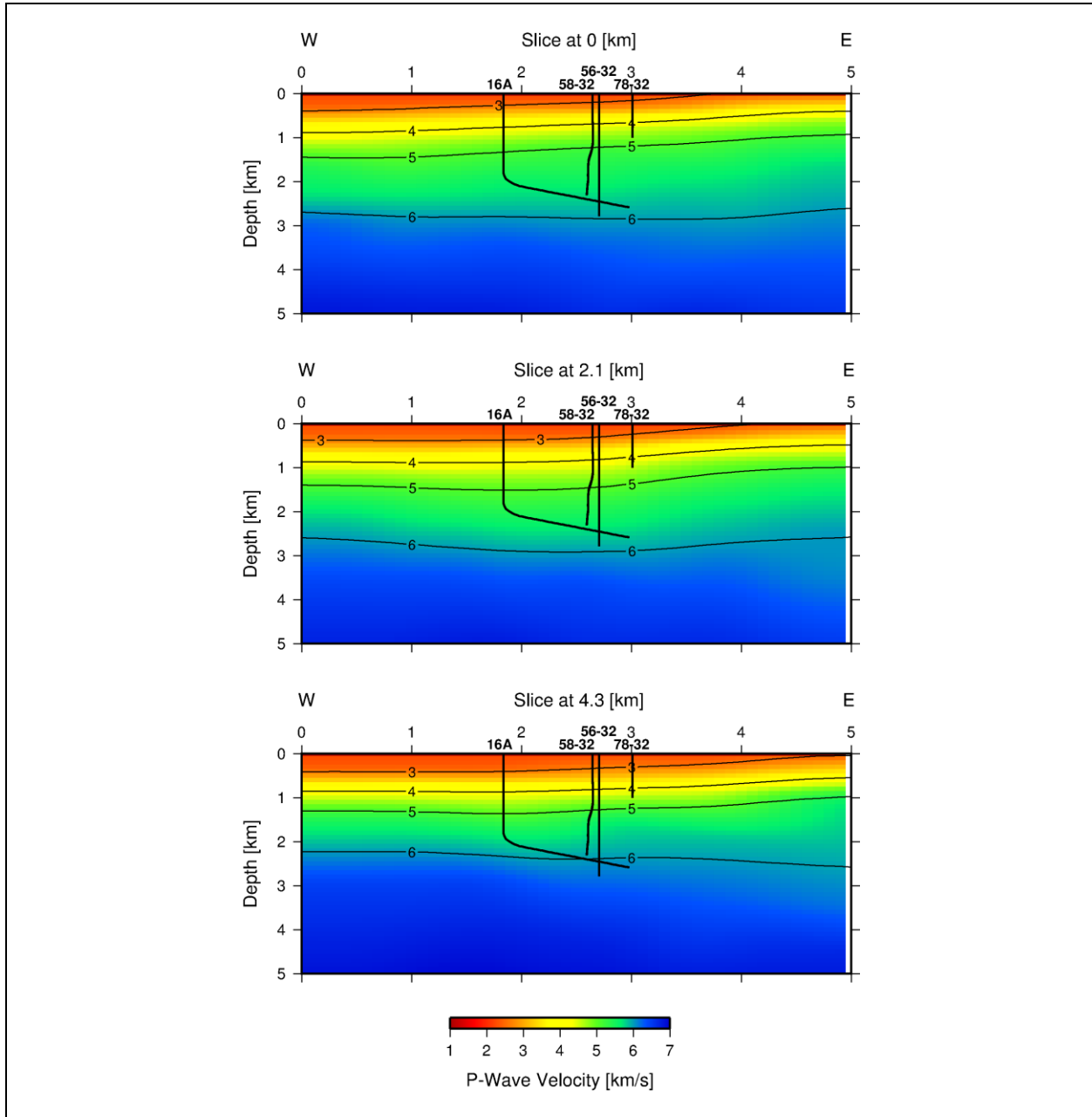

Figure 3. East-west cross section through the 3D velocity model obtained from scaled RMS velocities of the seismic reflection survey. The location of each cross sections is noted at the top of the panels and refers to the north-south coordinate in Figure 1. The wells are shown for reference.

A section of the seismic reflection survey is presented in Figure 4. It shows an east-west cross section through the center of the FORGE site. The basement interface is characterized by a strong reflection dipping from east to west, which is recovered in the velocity model in Figure 3. The dip of the interface in both figures is different due to the difference in vertical scale.
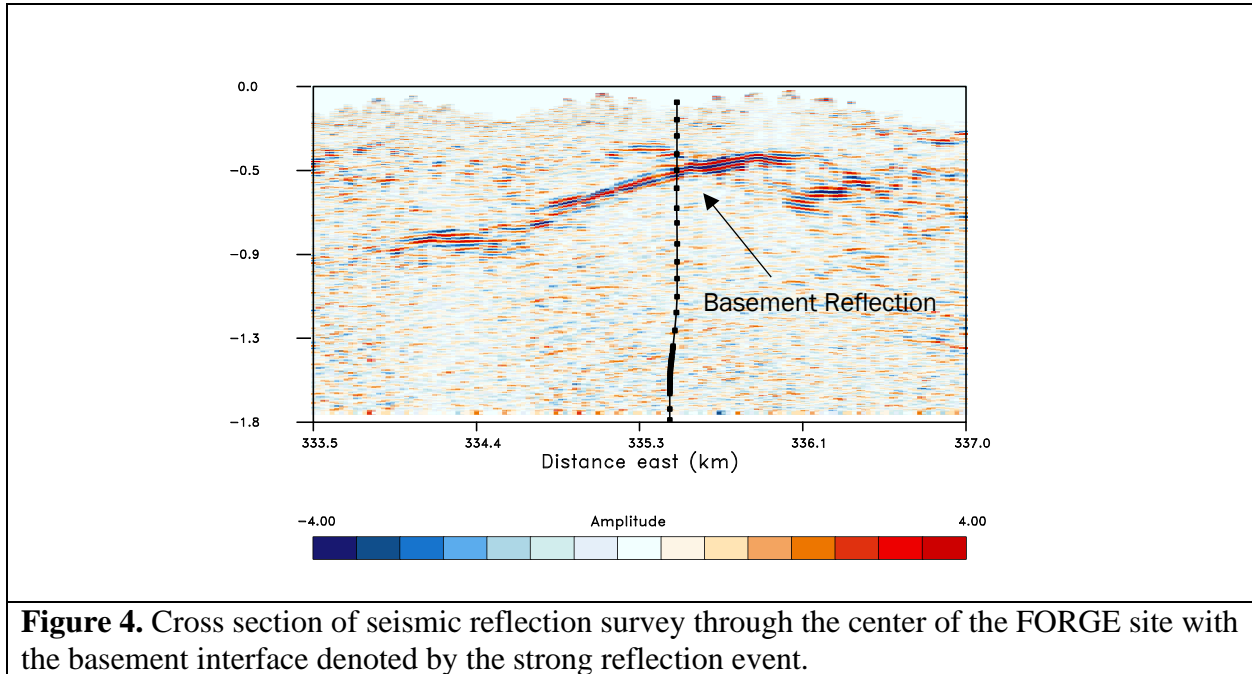

Figure 4. Cross section of seismic reflection survey through the center of the FORGE site with the basement interface denoted by the strong reflection event.

Because the velocities of the reflection survey are less reliable in the shallow sediments, and logs are not available for the shallow subsurface, it was decided to estimate the arrival times of the direct P-waves from the reflection data and inverting these data to obtain P-wave velocities. The direct P-waves are well suited to estimate the velocity in the shallow subsurface because they refract off the basement interface and mainly propagate in in sedimentary layer. Data processing was based on the software package PhaseNet (Zhu and Berosza, 2019), a deep-neural-network-based seismic arrival time picking method. PhaseNet uses seismic waveform data as input and outputs probability distributions of seismic arrival times. The maxima in the probability distributions provide accurate arrival times for the seismic waves. In the current case, 93 preliminary source locations were used to test PhaseNet on the seismic reflection data. The location of the 93 sources are denoted by the red open circles in Figure 1, which were chosen to provide sufficient coverage of the survey area. The initial velocity model in Figure 3 was used to compute time windows on the waveforms for PhaseNet to estimate arrival times of the direct P-wave velocity. The data processing resulted in 98,000 P-wave travel times for the set of preliminary source positions. The travel times were subsequently inverted with tomoFDD to update the initial velocity model. tomoFDD is an inversion code that performs joint inversion for earthquake locations and for 3D P- and S-wave velocity structure (Zhang and Thurber, 2006; Gritto et al., 2013). In the current case the code was used to update the P- and S-wave velocity model only, since the source locations are known. The S-wave velocity model, not shown here, was generated through scaling by a Vp/Vs ratio of 1.73.

4

The result of inverting the P-wave travel times is presented in Figure 5, which shows cross section at the same locations as in Figure 3. The comparison between the two models reveals differences in the upper section of the model down to approximately 1.5 km depth. This is resulting from the propagation of the direct P-waves, which are confined to the sediments and the upper basement.
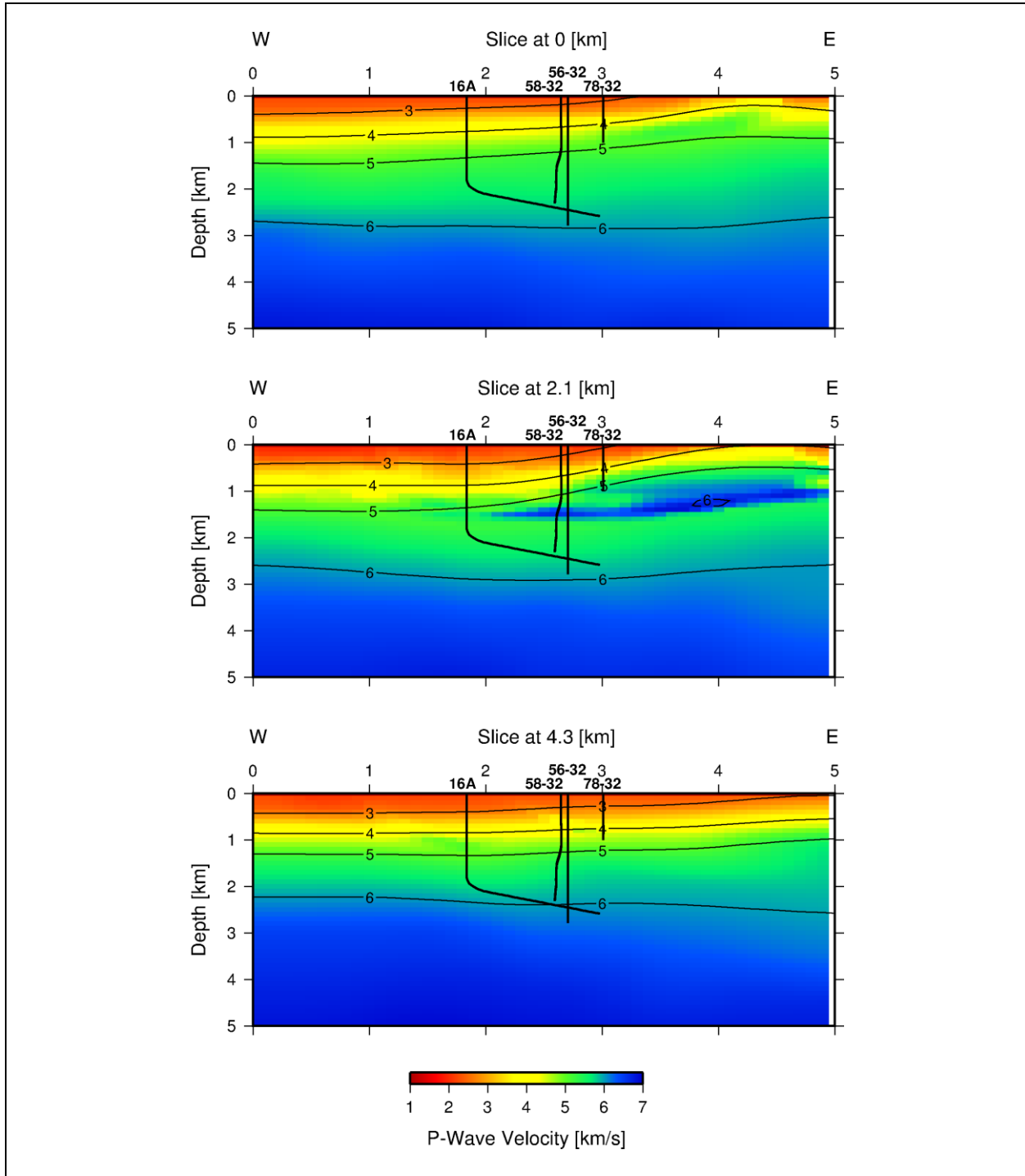

Figure 5. East-west cross section through the 3D velocity model resulting from the inversion of 98,000 P-wave travel times.

Because of the P-wave propagation in the sedimentary layer, in Figure 6, the results of the velocity estimates are shown only at those nodes that have sufficient resolution as defined by the derivative weight sum (DWS). DWS represents a measure of the total ray density at each node (Thurber and Eberhart-Phillips, 1999) and is a reasonable proxy for resolution (Zhang and Thurber, 2007).
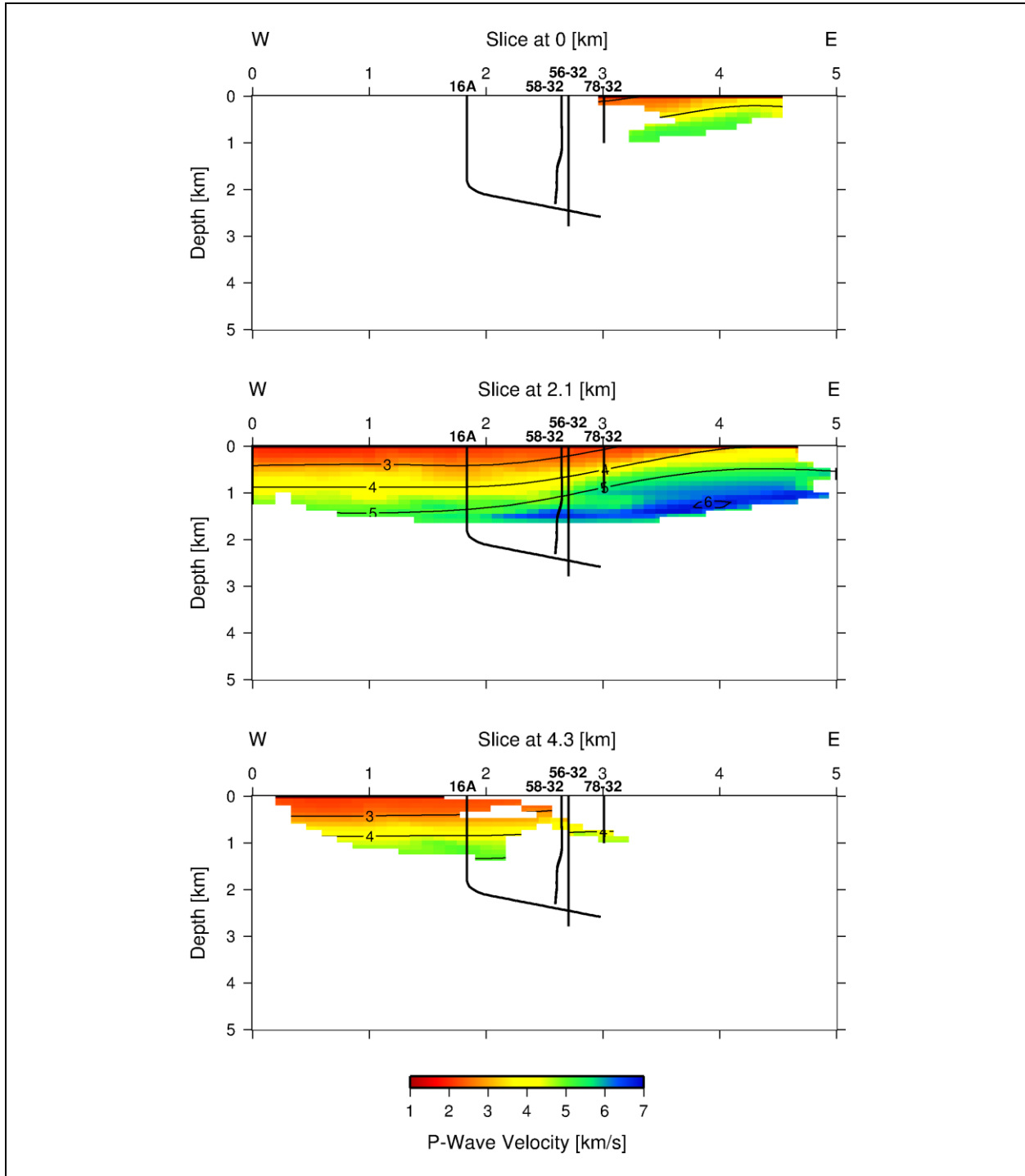

Figure 6. East-west cross section through the 3D velocity model resulting from the inversion of 98,000 P-wave travel times. Shown are only those areas with DWS ≥ 0.1.

The limit for plotting velocity estimates in Figure 6 is set to 0.1 on a normalized scale of the DWS (i.e., DWS ≥ 0.1). Areas with insufficient resolution are plotted white. Only the sedimentary layer is resolved throughout the central regions of the survey area, while the extreme transects on the northern and southern end of the survey area are poorly resolved owning to the geometry of the source and receiver lines (Figure 1). A map view of the differences between the initial and inverted 3D velocity model is presented in Figure 7a. The differences are only shown down to 1.5 km depth, the limit in resolution of the inverted model. In the western region the inversion produces lower velocities compared to the initial model, while in the easter half the velocities are higher compared to the initial model. The static corrections for each receiver location are plotted in Figure 7b. The results indicate that there is no systematic shift in statics across the survey region.
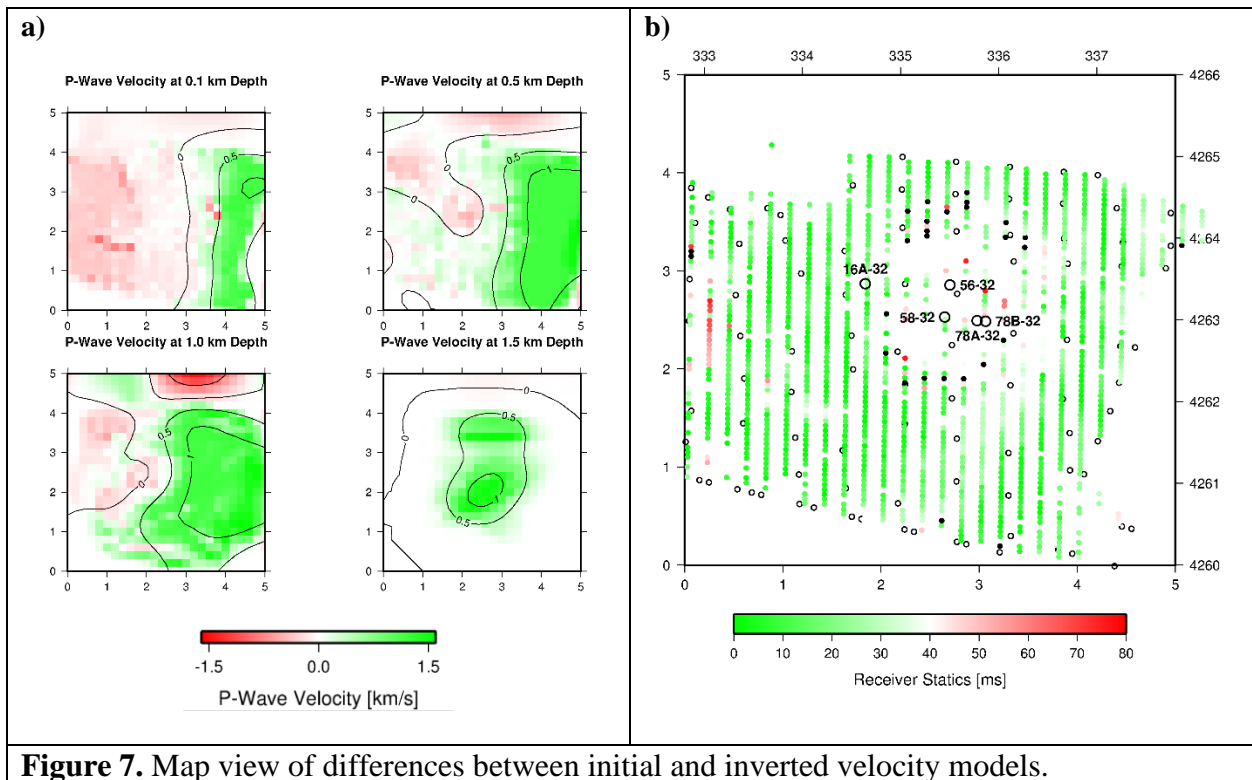

Figure 7. Map view of differences between initial and inverted velocity models.

The results suggest that the velocities of the shallow sediments in the initial model are too high. This may result from scaling the RMS velocities to match the logging velocities in the initial stage of the model building. It is known that estimates of velocities derived from logging measurements tend to be higher than those from surface experiments, due to differences in scale of the seismic wavelengths of these techniques.

At present, we are developing a new 3D velocity model, based on an initial model with slower sedimentary velocities and slightly lower basement velocities. This slower velocity model should also improve the results of determining P-wave arrival times, because the time windows for the application of PhaseNet become more accurate. Additionally, we are moving ahead generating larger volumes of P-wave arrival times by including more vibroseis source locations. The final model will be included in the milestone report for Task 3.2

3. Preliminary Resolution Analysis of Seismic Wave Propagation in the Reservoir (Task 3.2)

The goal of Task 3.2 is to estimate the seismic resolution in the stimulated reservoir, evaluating the potential for future seismic imaging campaigns to reliably image the generated fracture network. In the current analysis, we use the seismicity recorded during Stage III of the reservoir stimulation in well 16A(78)-32 in April 2022, because the geometry of the stimulation experiment is similar to what is planned during the next stimulation in well 16B(78)-32. Therefore, the seismicity recorded during Stage III of the last stimulation serves as a proxy for the data of the future experiment.

The locations and trajectories of the injection well and the geophysical observation wells is presented in Figures 8 and 9. The injection well 16A(78)-32 is vertical to 1,800 m depth, after which it is deviated to the southeast until it reaches a final depth of 2,600 m. The geophysical observation wells are mainly vertical and reach depths between 1,000 m and 2,900 m. Twenty-one seismic sensors, indicated by the red crosses in Figures 8 and 9, were located in the observations wells within the granitic basement. The Stage III stimulation generated a seismic cloud of which 1,526 events were analyzed and located by Geo-Energie Suisse AG (GES) and which are shown by the black dots in Figures 8 and 9 (Pankow, 2022). The data analysis yielded 28,773 P- wave and 26,778 S-wave phase arrivals, which were subsequently used to estimate the seismic resolution in the stimulated volume.
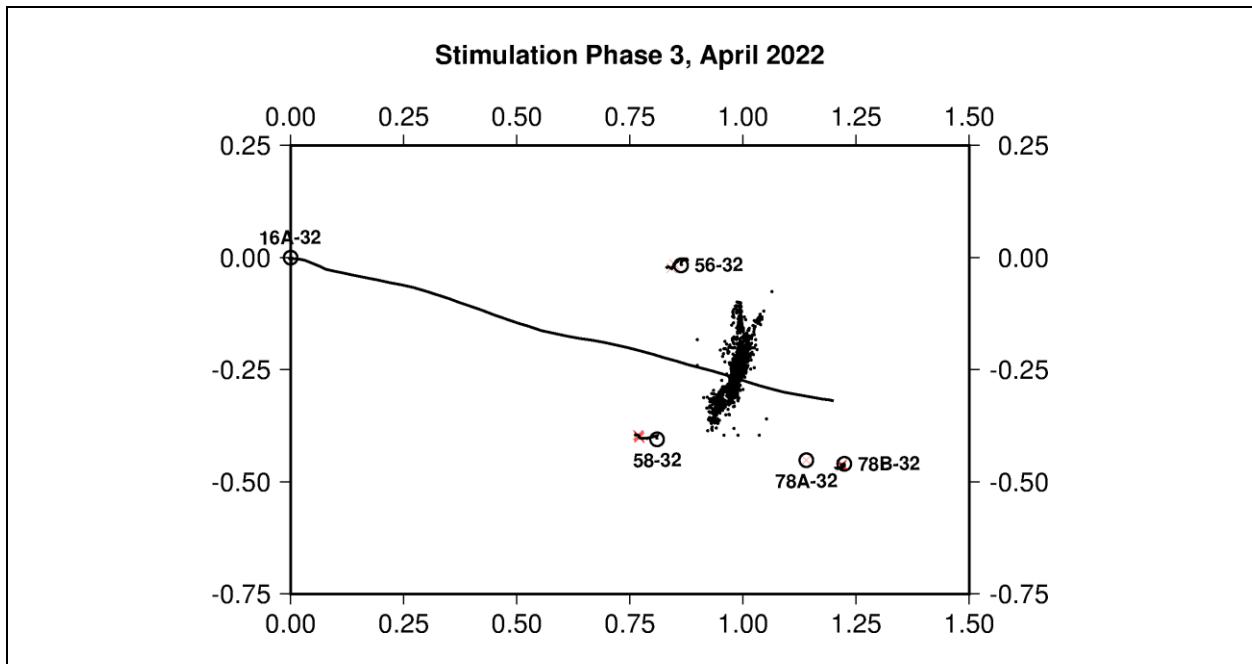

Figure 8. Map view with the locations and trajectories of the injection (16A-32) and geophysical observation wells (56-32, 58-32, 78A-32, 78B-32) at the FORGE site. The seismic sensors in each well are denoted by red crosses, while the seismicity recorded during Stage III of the April 2022 stimulation is given by the black dots.
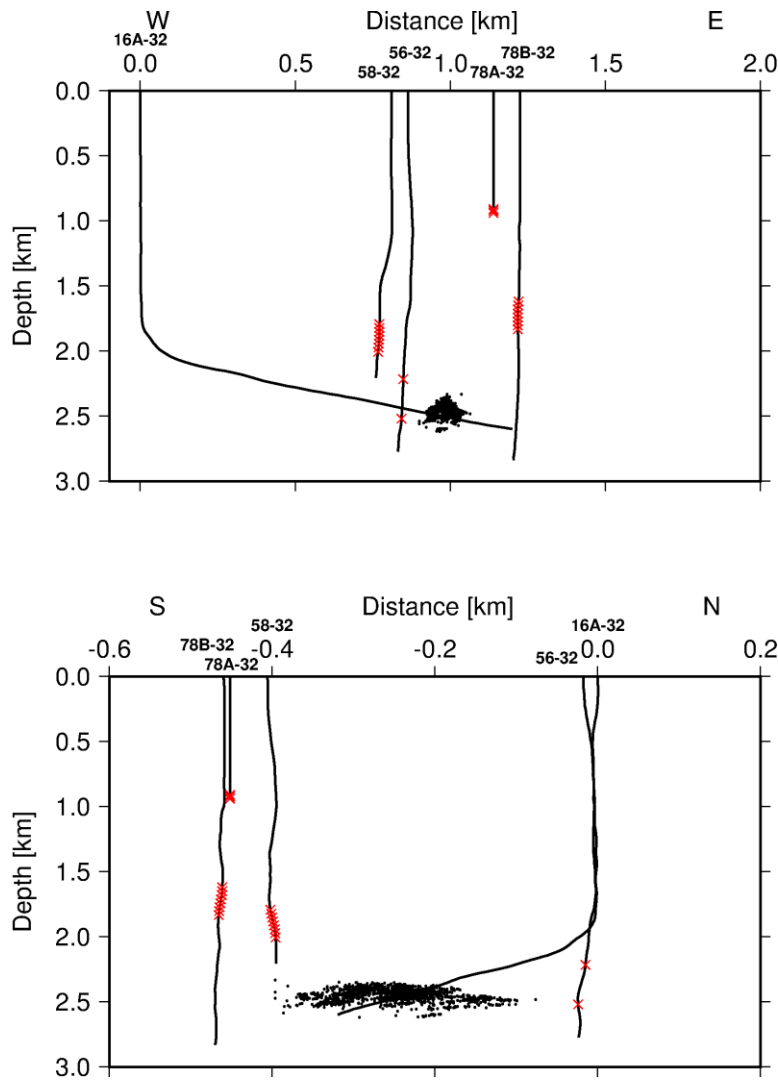
Figure 9. Vertical cross sections through the FORGE site with the geometry of the injection well 16A-32 and the geophysical observation wells 56-32, 58-32, 78A-32, and 78B-32. The seismic sensors in each well are denoted by red crosses. The seismicity recorded during Stage III of the April 2022 stimulation is given by the black dots.

For the resolution analysis, a homogeneous velocity model was assumed, because the seismic sensors were all located in the granitic basement, which is comprised of competent rock. The velocity values were the same as those used by GES for the analysis and location of the induced earthquakes (Vp = 5.83 km/s, Vs = 3.41 km/s). Using the earthquake hypocenters, the velocity model, and the sensor locations, seismic ray tracing was performed using the eikonal solver (Podvin and Lecomte, 1991) of the program tomoFDD, which returned DWS values of the seismic velocities in the stimulated fracture volume. Gritto and Nihei (2019) showed that the normalized qualitative resolution estimates of DWS are equivalent to quantitative resolution estimates based on singular value decomposition (Vasco, 2003). In seismic imaging it is generally accepted that a resolution of 0.1 is sufficient to reliably image the structure under investigation (i.e., Thurber et

al., 2009; Lin et al., 2015). In the current task, we require a limit of DWS ≥ 0.2 to satisfy the threshold for resolution in the stimulated volume.

The preliminary results of the resolution analysis are presented in Figure 10, which shows a 3D view of the well geometries and seismicity at the FORGE site as well as the DWS of the P- and S-waves in the stimulated region. The seismic sensors are denoted by the gray cubes along the borehole trajectories, while the DWS is given by the colored cubic symbols. In the figures only values with a DWS ≥ 0.2 are plotted. It can be seen that the resolution is highest near the sensors, where the concentration of raypaths is densest. The resolution decreases with increasing distance from the sensors until it increases near the cloud of earthquakes again. In the stimulated volume, the resolution is equal or greater than the threshold of DWS ≥ 0.2. The P- and S-wave resolution is nearly identical except for the sensors in borehole 78A-32. Due to the distance of the sensors in 78A-32 from the stimulated volume, the signal-to-noise amplitude ratio (S/R) is low such that no S-wave phase arrival times were estimated.
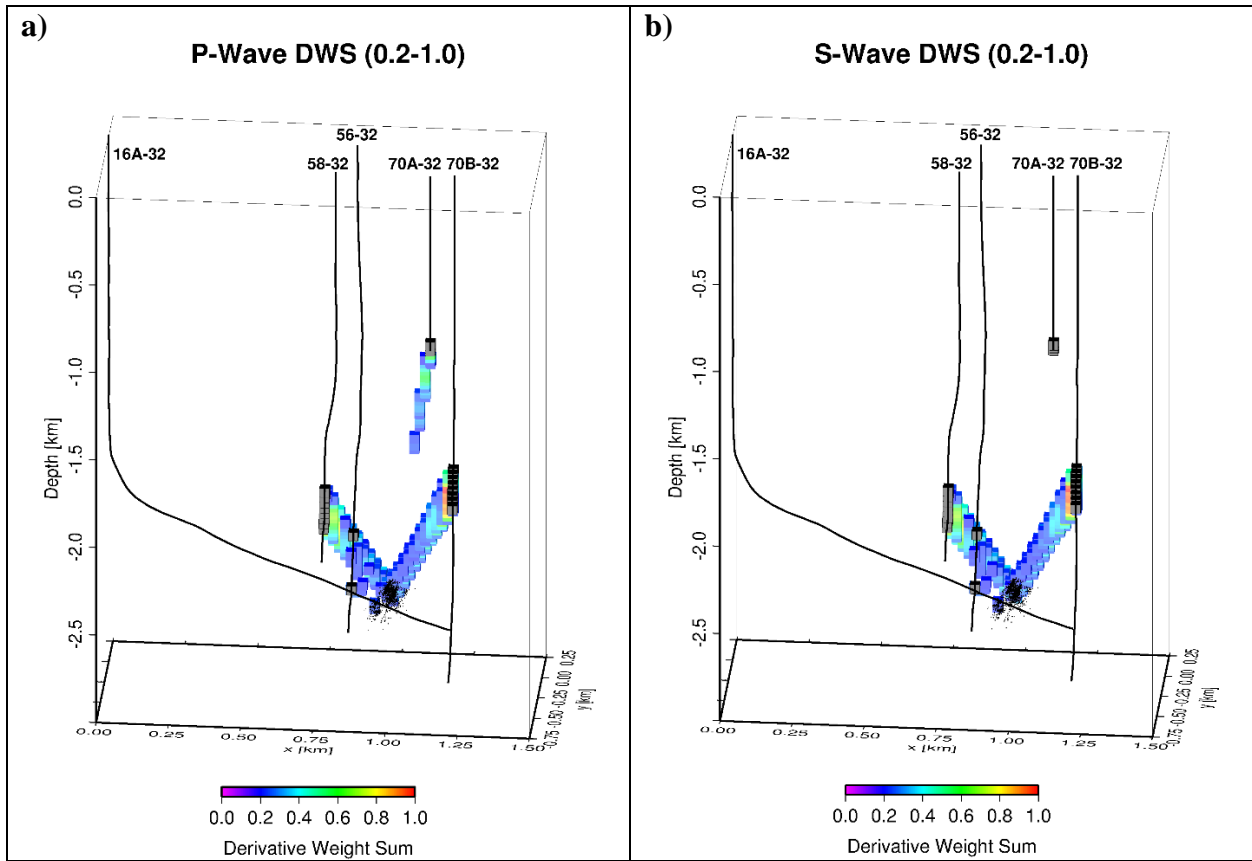

Figure 10. 3D view of the FORGE site displaying the trajectories of the injection and geophysical observation wells (black lines), the seismicity of the Stage III April 2022 stimulation (black dots), the seismic sensors (black cubes), and the DWS ≥ 0.2 for the **(a)** P-waves and **(b)** S-waves.

Figure 11 shows a similar 3D view, but for a plotting limit of DWS ≥ 0.5. At this higher threshold, the resolution is provided by the sensors in well 58-32, which are closest to the seismic cloud. It can be seen that some regions in the stimulated volume reveal DWS ≥ 0.5.
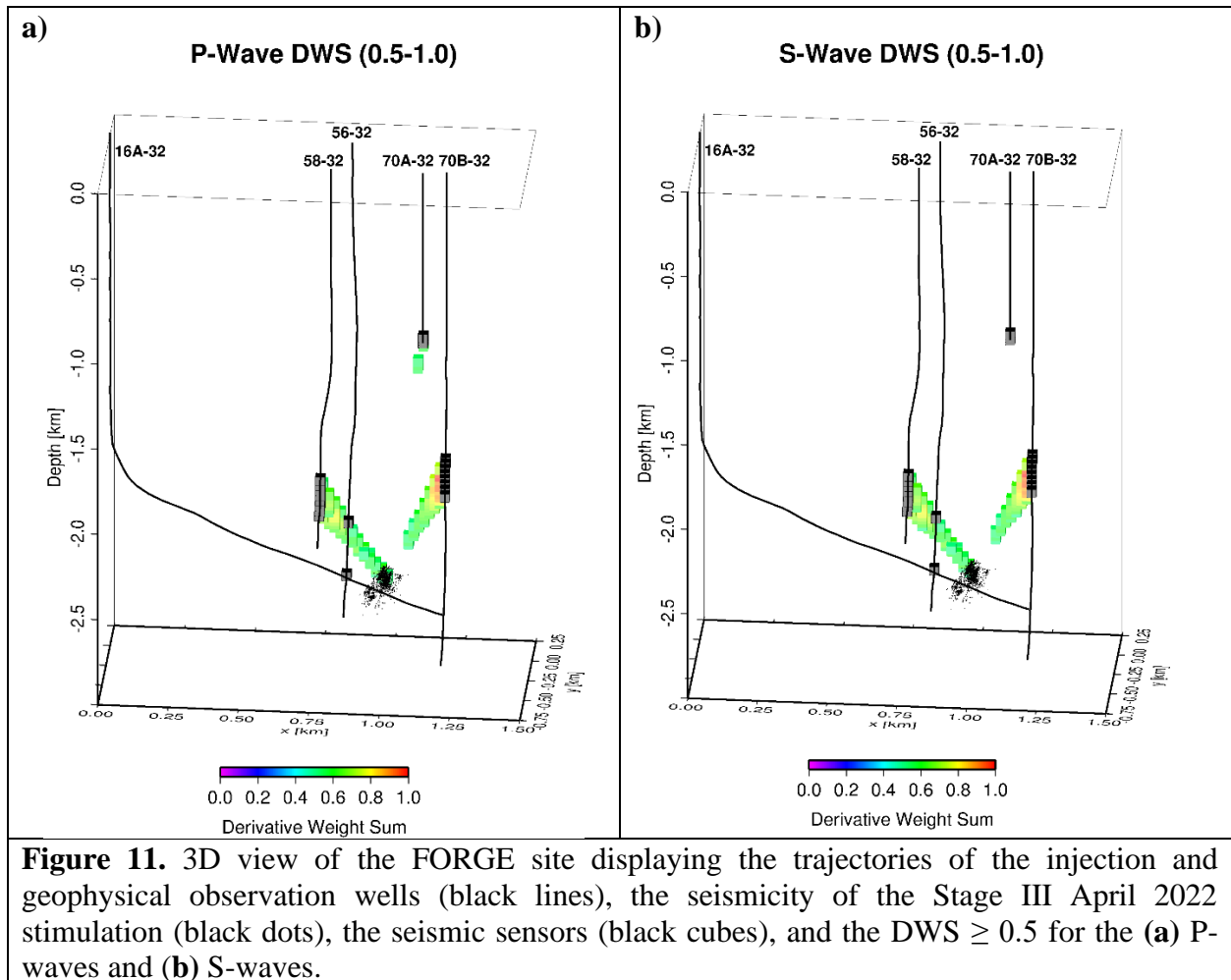

Figure 11. 3D view of the FORGE site displaying the trajectories of the injection and geophysical observation wells (black lines), the seismicity of the Stage III April 2022 stimulation (black dots), the seismic sensors (black cubes), and the DWS ≥ 0.5 for the **(a)** P-waves and **(b)** S-waves.

Similar results of the seismic resolution are presented in map view in Figure 12. The panels show horizontal sections through the FORGE area centered on the Stage III seismicity, with the surface locations of the observation boreholes and the trajectory of well 16A-32. The depth of the horizontal slices is denoted at the top of each panel. The seismicity in each panel, indicated by the black dots, represents projections of the earthquake hypocenters from 25 m above and below the depth of each panel. The first panel at 2300 m depth is located above the seismic cloud. Three resolution maxima are visible, which are associated with the P-waves propagating to the respective observation wells. As the depth of the panels increase into the seismic cloud, it can be seen that the maxima merge and the DWS level increases. The highest resolution (DWS ~ 0.5) is associate with the maximum seismic density at 2,400 m depth. As the panels dip below the seismic cloud the resolution quickly decays.

Figure 12. Map view of the P-wave DWS at different depth levels through the cloud of seismicity.
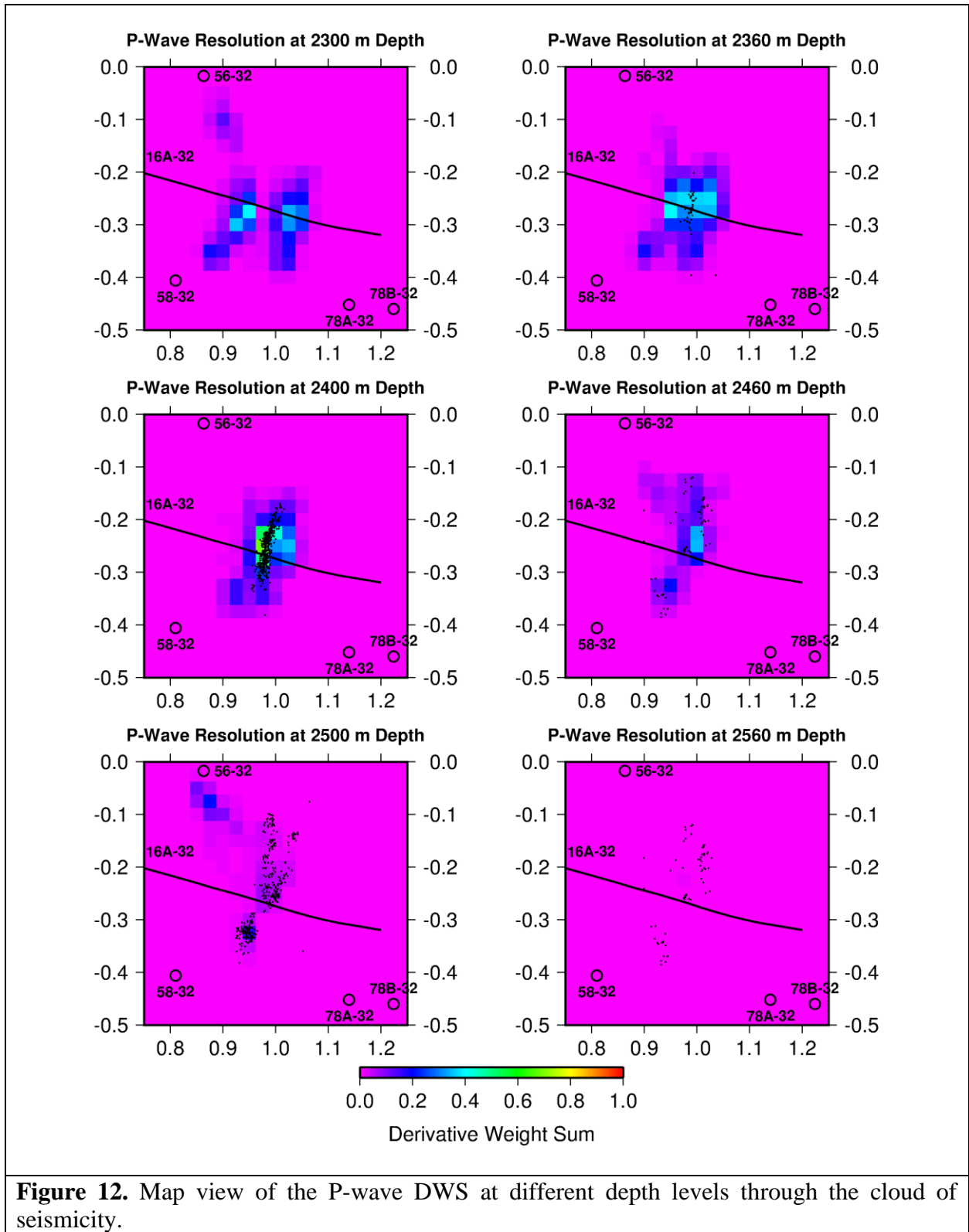
Similar results are observed in Figure 13 for the resolution of the S-waves. Maximum resolution of DWS ~ 0.5 are observed at 2,400 m depth. The results are comparable to the P-wave resolution, because the number of P- and S-wave phases, observed for the Stage III seismicity, is comparable.
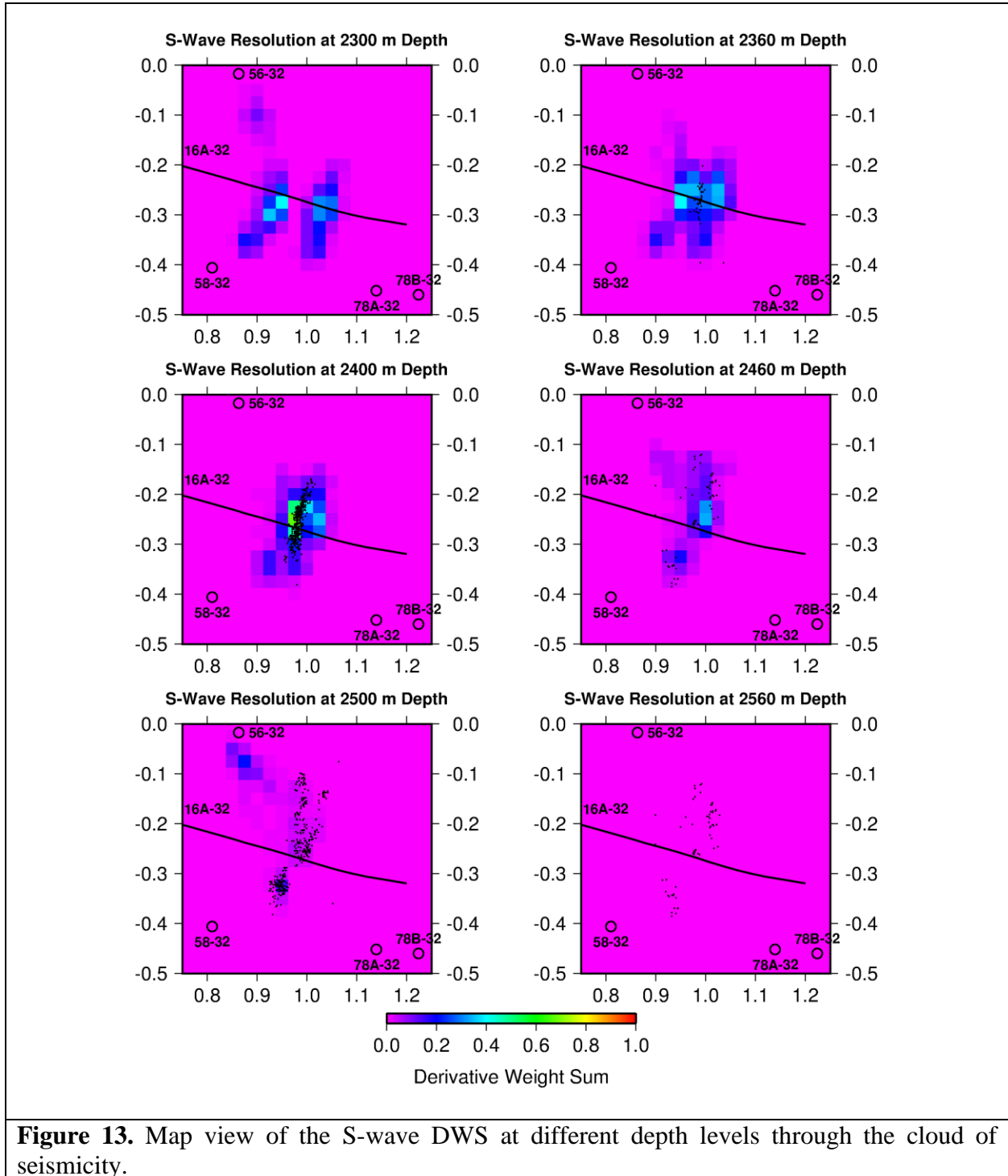

Figure 13. Map view of the S-wave DWS at different depth levels through the cloud of seismicity.

4. Conclusions and Future Work

A preliminary 3D velocity model for the larger FORGE area was developed using RMS velocities of the seismic reflection survey and seismic velocity logs from borehole measurements as an input model. To improve the accuracy of the model in the shallow subsurface, travel times phase arrivals of the direct propagating P-waves were determined from the seismic reflection data, using PhaseNet, a deep-neural-network-based seismic arrival time picking method. The travel times were subsequently inverted using the input velocity model. The results showed that the input velocity model needs improvement as the resulting model appears too fast in the easter region of the FORGE area. During the second phase of Task 3, we will update the input velocity model and generate P-wave arrival times for additional seismic source locations, to improve the horizontal resolution in the sedimentary layer and to obtain a model that better matches the sedimentary layer and the travel time observations.

The preliminary results of seismic resolution in the stimulated reservoir illustrated that the DWS of the P- and S-waves is sufficiently high to perform reliable seismic imaging. Throughout the cloud of seismic events in the stimulated region of the reservoir the DWS was found to range from 0.2 - 0.5, which is higher than the generally accepted imaging threshold of 0.1. During the second phase of Task 3.2, we will concentrate on incorporating additional sensors (i.e., DAS string and/or surface sensors) to investigate the potential for further improvement of the DWS.

5. References

Gritto, R., S.H. Yoo and S.P. Jarpe, 2013. Three-dimensional seismic tomography at The Geysers geothermal field, CA, USA, *Proceedings, 38th Workshop Geothermal Reservoir Engineering*, SGP-TR-198.

Gritto, R. and K.T. Nihei, 2019. High-Resolution Imaging of Geothermal Flow Paths Using a Cost-Effective Dense Seismic Network, Task 2: Dense Network Design, *Final Report*, California Energy Commission, EPC-16-021, pp. 1-21.

Lin, G., P. M. Shearer, F. Amelung, and P. G. Okubo, 2015. Seismic tomography of compressional wave attenuation structure for Kilauea Volcano, Hawai'i, *J. Geophys. Res*. Solid Earth, **120**, 2510–2524, doi:10.1002/2014JB011594.

Miller, J., 2019. Utah FORGE: Seismic Reflection Data. United States. https://dx.doi.org/ 10.15121/1542059.

Pankow, K., 2022. Seismic Data from the Well 16A(78)-32 Stimulation April, 2022. United States. https://dx.doi.org/10.15121/1879450.

Podvin, P., and I. Lecomte, 1991. Finite difference computation of travel times in very contrasted velocity models: A massively parallel approach and its associated tools, *Geophys. J. Int.,* **105**, 271–284.

Thurber, C. H., and D. Eberhart-Phillips, 1999. Local earthquake tomography with flexible gridding, *Comp. and Geosci.*, **25**, 809–818.

Thurber, C., H. Zhang, T. Brocher, and V. Langenheim, 2009. Regional three-dimensional seismic velocity model of the crust and uppermost mantle of northern California, *J. Geophys. Res.*, **114**, B01304, doi:10.1029/2008JB005766.

Vasco, D. W., L.R. Johnson and O. Marques, 2003. Resolution, uncertainty, and whole Earth tomography, J. Geophys. Res., 18, 2022, doi:10.1029/2001JB000412.

Zhang, H., and C. Thurber, 2007. Estimating the model resolution matrix for large seismic tomography problems based on Lanczos bidiagonalization with partial reorthogonalization, *Geophys. J. Int.*, **170**, 337– 345.

Zhang, H. and C. H. Thurber, 2006. Development and Applications of Double-difference Seismic Tomography, *Pure Appl. Geophys.*, **163**, DOI 10.1007/s00024-005-0021-y, 373-403.

Zhu W. and G. C. Beroza, 2019. PhaseNet: a deep-neural-network-based seismic arrival-time picking method, *Geophys. J. Int.*, **216**, 261–273 doi: 10.1093/gji/ggy423.